1 **Complexity**

2 **Multiple morphological constraints based complex gland**

3 **segmentation in colorectal cancer pathology image analysis**

4 Kun Zhang[1], JunHong Fu[1], Liang Hua[1], Peijian Zhang[1], Yeqin, Shao[2], Sheng Xu[3], Huiyu
5 Zhou[4]

6 [1] Department of Electrical Engineering, Nantong University, Nantong 226019, China.
7 [2] School of Transportation, Nantong University, Nantong 226019, China
8 [3] School of Electronic and Information Engineering, Nantong Vocational University, Nantong
9 226019, China.
10 [4] School of Informatics University of Leicester UK

11 Correspondence should be addressed to Kun Zhang; zhangkun_nt@163.com

12   Liang Hua; hualiang@ntu.edu.cn

Abstract

14 Histological assessment of glands is one of the major concerns in colon cancer grading.
15 Considering that poorly differentiated colorectal glands cannot be accurately segmented, we
16 propose an approach for segmentation of glands in colon cancer images, based on the
17 characteristics of lumens and rough gland boundaries. First, we use a U-net for stain separation
18 to obtain H-, E-, and background stain intensity maps. Subsequently, epithelial nucleus is
19 identified on the histopathology images, and the lumen segmentation is performed on the
20 background intensity map. Then, we use the axis of least inertia based similar triangles as the
21 spatial characteristics of lumens and epithelial nucleus, and a triangle membership is used to
22 select glandular contour candidates from epithelial nucleus. By connecting lumens and
23 epithelial nucleus, more accurate gland segmentation is performed based on the rough gland
24 boundary. The proposed stain separation approach is unsupervised, and the stain separation
25 makes the category information contained in the H&E image easy to identify and deal with the
26 uneven stain intensity and the inconspicuous stain difference. In this project, we use deep
27 learning to achieve stain separation by predicting the stain coefficient. Under the deep learning
28 framework, we design a stain coefficient interval model to improve the stain generalization
29 performance. Another innovation is that we propose the combination of the internal lumen
30 contour of adenoma and the outer contour of epithelial cells to obtain a precise gland contour.
31 We compare the performance of the proposed algorithm against that of several state of the art
32 technologies on publicly available datasets. The results show that the segmentation approach
33 combining the characteristics of lumens and rough gland boundary have better segmentation
34 accuracy.

Introduction

36 Colon cancer may be caused by epithelium (lumens of blood vessels, organs and surface
37 tissues), also called adenocarcinoma (malignant tumor formed by gland structures in epithelial

38 tissues) [1]. It affects the distribution of cells and also changes the structure of glands.
39 Pathologists are able to accurately detect small abnormalities in a biopsy [2-4].

40 With the increasing popularity of histopathology images, digital pathology provides a viable
41 solution to the detection problem. Histopathology image analysis can help us to extract
42 quantitative morphological features and can be used for computer-assisted cancer grading [5].
43 Histopathology is the fixation of thin sections of potentially disease tissues on a glass slide and
44 stain to show specific structural or functional details [6-7]. By scanning the entire slide with a
45 scanner, digitized images of those slides can be obtained, making histopathology suitable for
46 image analysis [8-9].

47 Colon histopathology image analysis is the basis of the primary detection of colon lesions [10].
48 The gland structure is shown in Figure 1a. A typical colon gland histopathology image contains
49 four tissue components: lumen, cytoplasm, epithelial cells, and stroma (connective tissues,
50 blood vessels, nerve tissue, etc.). The lumen area is surrounded by an oval structure called
51 epithelial cells [11-12]. The whole structure is bounded by a thick line, called the epithelial cell
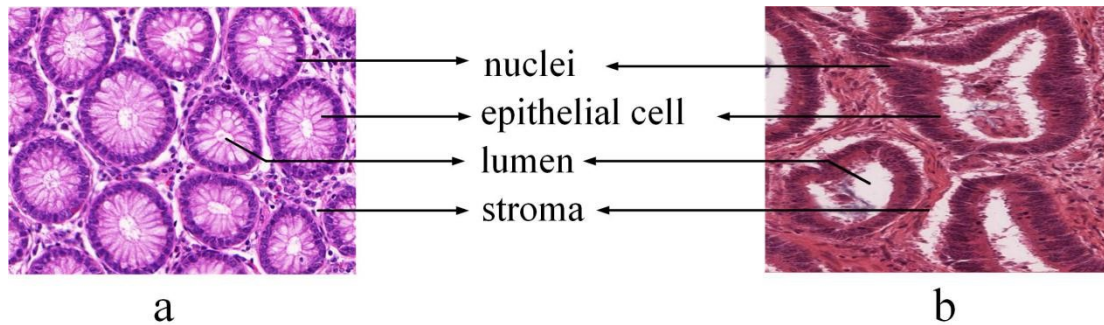52 nucleus.

53

54 Figure 1 Illustration of colon images: (a) A typical benign colon gland histopathology image and its composition.
55 (b) A malignant colon gland image.

56 In clinical practice, pathologists use glands as the objects of interests, including their structural
57 morphology and gland formation [13-14]. Especially, when performing automated gland
58 segmentation in H & E images, pathologists can extract important morphological features to
59 determine prognosis and plan treatments for individual patients [15]. Digital histopathology
60 images contain noise and homogenous regions that hinder gland detection and segmentation.
61 For example, Kerekes et al. [16] developed two diagnostic modules, one for gland detection
62 and the other for nuclei detection. In gland detection, HSV and LAB color spaces are used for
63 color segmentation, and glands can be identified using the connected component approach
64 reported in [54]. Due to large differences between the tissue preparation protocols, stain
65 programs and scanning characteristics, stain normalization of histopathology images provides
66 a tool to ensure the efficiency and stability of the system. Cheikh et al. [17] used a
67 normalization technique to associate the mean and standard deviation of each channel of the
68 target tissue image with those of the template image through a set of linear transformations in
69 the LAB color space. In order to segment a large number of color images into meaningful
70 structures, Banwari et al. [18] proposed a thresholding approach based on image intensity.
71 These approaches are based on different tissue structures and color differences and are not
72 suitable for segmenting adherent glands or glands that are mixed with stroma which require
73 complex correction algorithms to obtain accurate results. The active contour segmentation
74 approach proposed by Cohen [19] relies on the characteristics of the gland structures. The

2

75 thickness of the tissue slice and the fading of the stain will lead to the change of the color
76 distribution of the tissue image, and the gland model is not suitable for the glands with
77 incomplete gland boundaries. The above conventional approaches mainly used glands'
78 appearance characteristics and features. The appearance characteristics are composed of the
79 nucleus, cytoplasm and epithelial cells. Sirinukunwattana [20], Jacobs [21] and others used
80 low-level features: color, texture and edges to identify glands. The contour features are based
81 on a gland structure surrounded by epithelial cells. Sirinukunwattana [22] and Fu et al. [23]
82 proposed that the spatial random field model well segmented the benign gland contour, but it
83 was not suitable for segmenting malignant and diseased glands.

84 With the recent development of deep learning in the field, it has become possible to apply deep
85 learning to histopathology images. Roth et al. [24] proposed a multi-level deep convolutional
86 neural network for automated pancreatic segmentation. Ronneberger [25] and others proposed
87 to use U-net for histopathology image segmentation. The deep contour sense network proposed
88 by Chen et al. [26] illustrates that contours play an important role in gland segmentation. The
89 double parallel branch deep neural network proposed by Wang et al. [27] combined contours
90 and other features to accurately segment glands. In addition, Xu et al. [28] proposed a fusion
91 of complex multi-channel regions and boundary modes for segmentation of gland instances by
92 side supervision. This work was extended in the study of Xu et al. [29], which included
93 additional information to enhance performance. Raza et al. [30] proposed a multi-input
94 multiple-output network (MIMO-Net) for gland segmentation and achieved state-of-the-art
95 performance. All of the above approaches require a large number of manual annotations, but it
96 was very difficult to label a large number of histopathology images. Zhang et al. [31] used a
97 deep confrontation network for unannotated images, achieving consistently good segmentation
98 performance.

99   Although the previous approaches has achieved certain promising results in gland
100 segmentation, automated segmentation of glands is still a challenging task due to the
101 complexity of histopathology images and the diversity of gland morphology, especially the
102 gland lesions showed in Figure 1b. For normal glands, epithelial cells can be clearly
103 distinguished from the surrounding environment [32]. For malignant glands, epithelial cells are
104 usually intermingled in the stroma, and the epithelial nucleus are not easily distinguished from
105 stromal nucleus [33], and even glands are attached to each other. In this situation, we consider
106 that the lumen is a defined structure of the gland. This structure can help decision making
107 because its presence and morphology indicate the grade of cancers [34]. It is observed that the
108 lumen of the gland and the gland boundary have certain similarities in shapes, and the lumen
109 can be accurately segmented compared to other structures of the gland. Afterwards, a gland
110 segmentation approach based on the correlation between the lumen and the gland boundary
111 was proposed.

112 Our proposed approach first uses a U-net for stain separation to obtain H-, E- and background
113 stain intensity maps. Subsequently, epithelial nucleus are identified on the histopathology
114 image. Taking into account that the lumen is similar to the background, shown in Figure 2. The
115 histopathology image is then used as the input of the framework proposed in [35] to obtain the
116 rough gland boundary and epithelial nucleus, and the lumen is segmented based on the
117 improved SPF approach reported in [36]. Finally, based on the correlation between the lumen
118 and the gland boundary, we select the best gland contour from the candidate contours so as to
119 achieve the segmentation of glands attached to each other. The innovation in our method is that
120 we are the first to use deep learning to achieve stain separation. Deep learning is used to predict
121 the stain coefficients. In the deep learning framework, we design a stain coefficient interval

122 model using Gaussian distribution. We can get a interval of the coefficient instead of a certain
123 stain coefficient to improve the stain generalization performance. Another innovation is we use
124 multiple morphological constraints to find the optimal tumor contour based on the internal
125 (lumen) and external (epithelium) contours .The proposed approach is evaluated on the 2015
126 MICCAI GlaS Challenge dataset and colon adenocarcinoma dataset, resulting in satisfactory
127 segmentation outcomes.

128
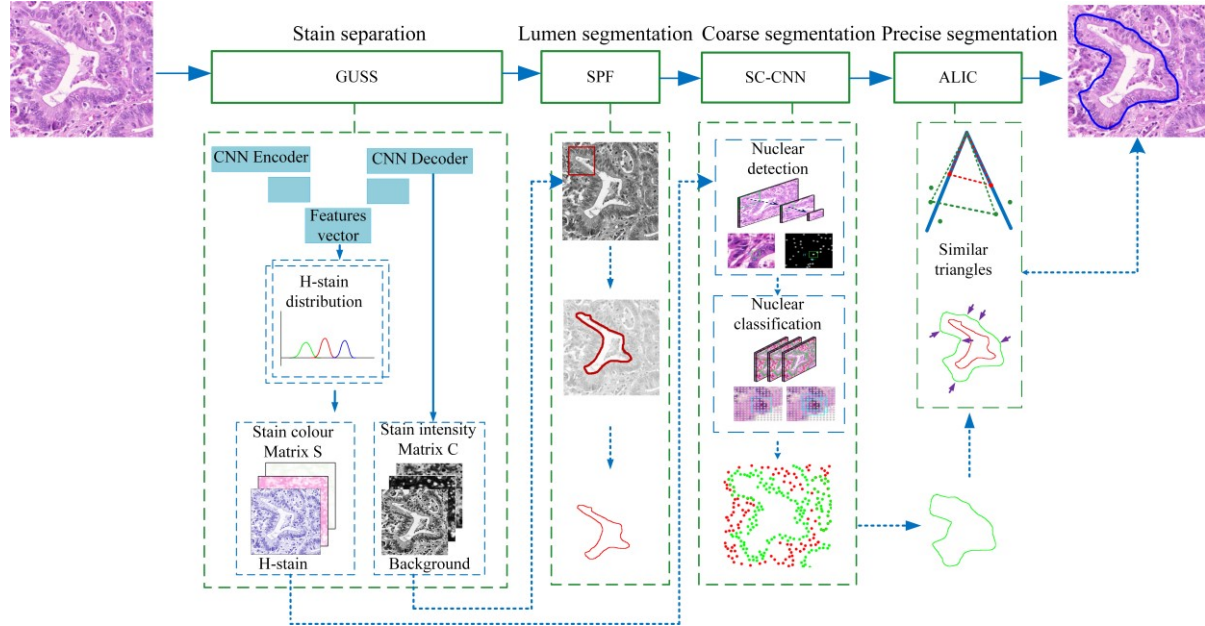
129 Figure 2: The architecture of the proposed approach.

130 **Materials and Methods**

131 **Histopathology image stain separation based deep learning framework**

132 The proposed stain separation framework is showed in Figure 3. Gaussian U-net Stain
133 Separation (GUSS) makes the information contained in H & E images easy to identify, thus
134 overcome the influence of uneven staining intensity or large differences in H & E
135 images.Traditional stain separation methods require manual settings for a standard stain matrix,
136 and cannot separate multiple stains at the same time. We here use deep learning to achieve this
137 function. First, the histopathology image is used as the input of the model, and the U-shaped
138 encoder-decoder model [55] is constructed for stain separation. The network is supported by
139 three parts: contracting, bridge and expanding paths to complete the stain separation of H
140 (Hematoxylin), E (Eosin) and B (Background) channels. The contracting path is used to reduce
141 the spatial dimension of the feature map, while increasing the number of the feature maps layer
142 by layer [37-40], extracting the input image as a compact feature. The bridge connects the
143 contracting and expanding paths. This U-shaped encoder-decoder model is improved to be a
144 multiple tasks model, besides the output of the U-net, we also use the most compact features
145 to predict the stain color matrixes, which is combined with mean and variance of stain color
146 values of Hematoxylin, Easin and Background paths. The expanding path is used to gradually
147 recover the details of the target and the corresponding spatial dimensions, and the output is
148 used for the prediction of the pixel-wise intensity map. The network is divided into ten residual
149 branches. Prior to each residual branch of the expanding path, there is a cascade for the
150 upsampling from the lower level feature maps and the feature maps from the corresponding

4

151 contracting path. The existence of the residual unit effectively avoids the problem of gradient
152 disappearance during the backpropagation [41]. In addition, each residual branch included
153 Convolution, Max Pooling, BN (Batch normalization) and ReLU (Rectified Linear Unit),
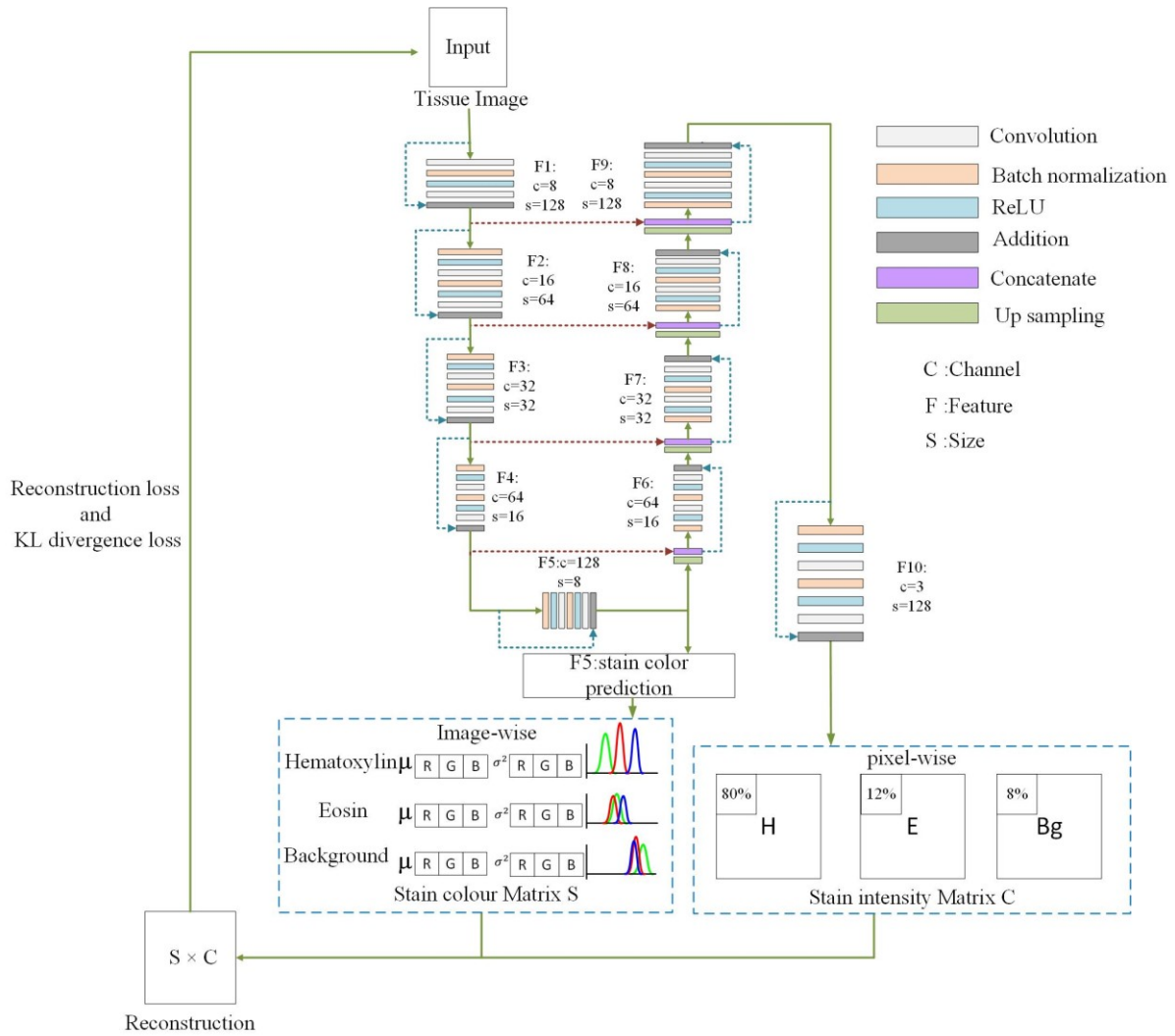154 which effectively accelerate the convergence speed [42].

155

156 Figure 3: The stain intensity map of hematoxylin-, eosin- and background channels is obtained from the
157 histopathology image by the proposed stain separation framework.

158 The model is trained by minimizing the reconstruction loss between the input image and each
159 reconstructed outcome, The original image goes into a 10-branch called F1-F10 network for
160 stain separation. The contracting path is composed of the first 1-4 branch network, and the fifth
161 branch is the bridge connecting the contracting and expanding paths, implementing the stain
162 color matrix prediction function. The expanding path consists of the 6th-9th branch network,
163 and the tenth branch output is used for stain intensity matrix prediction. In the stain color matrix
164 prediction, the F5 features are first flattened into a vector, and two fully connected layers are
165 deployed, with an intermediate node of 500 and an output node of 9, representing the R, G, and
166 B distributions of the three stain channels. During the training, the proposed predicts the stain
167 concentrations for each pixel as well as the parameters (mean and variance) of a series of
168 Gaussian distributions sampled to form an estimate of the stain matrix.

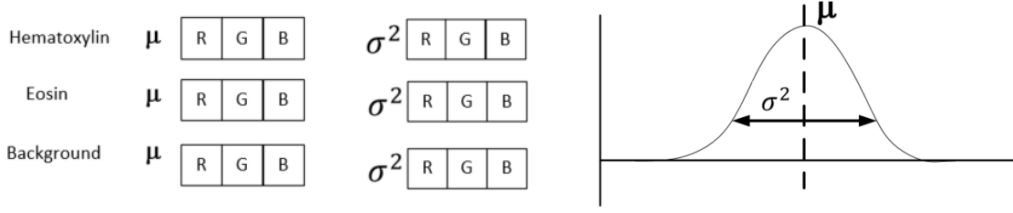169 Figure 4 shows an example of this process.

5

170

Figure 4: Stain mean and variance of the colour matrix.

For each of the stains contained in the image, the proposed method predicts 3 distributions - one for each of the RGB colour channels. The kth probability distribution $P_k = N(\mu_k, \sigma_k)$ may represent the red value of the hematoxylin stain. We use a value $h_R \backsim P_k$ to form an estimate of the red value of hematoxylin. This process is repeated for each of the distributions which are combined to form the estimated stain matrix S. The mean of each distribution μ_k represents the value around which our model has assigned the most probability whilst the standard deviation σ_k describes how certain the model where a value is sampled from will result in a low reconstruction error.

Taking the example above, we again assume that $P_k = N(\mu_k, \sigma_k)$ is the distribution representing the red value of hematoxylin; if $\mu_k = 0.5$ and the standard deviation is low, then the value we sample from P_k has a high chance of being close to 0.5. If the true red value of hematoxylin is close to 0.5, then the sampled value results in a reduced reconstruction loss; consequently, if the true red value is far from 0.5, then the sampled value will result in a very high reconstruction loss. If the model predicts a large standard deviation, the sampled value will vary greatly and produce a large reconstruction loss even if the mean value is correct. To find the optimal values for S, each of the mean values μ_k are close to the true values and the standard deviations σ_k are low.

For the stain separation task, in order to test the separation effect, the following loss function is defined:

$$Loss = \frac{1}{MN} \sum_{m=1}^{M} \sum_{n=1}^{N} \left(x_{n,m} - x'_{n,m} \right)^2 \tag{1}$$

In the formula, $x_{n,m}$ represents the nth pixel of the mth image, $x'_{n,m}$ represents the predicted image pixel.

Features are extracted from the histopathology image by the network described above, and then passed to a number of sub-branches that predict the intensity of the stain of each pixel and the parameters (mean and variance) of a series of Gaussian distributions. For each pixel in the image, R,G,B of the three channels (hematoxylin, eosin, background) are predicted.

Segmentation of lumens from the background channel based on the SPF-level set method.

Considering that lumens are one of the key components to distinguish glands, we segment lumens from the background channel after the stain separation. The SPF (Symbol Pressure

202   Function) is constructed by using the statistical information of the image, so that the SPF has
203   the function of maintaining or even enhancing the prominent foreground target. Similar to the
204   classical C-V model [43], the contour C allows us to divide the image I into two parts, inner
205   and outer, respectively, and uses the global intensity distribution of the image to construct the
206   SPF function. The stain intensity distribution functions of regions Ω_1 and Ω_2 are represented
207   by P_1 and P_2:

208

$$P_1(I, u_1, \sigma_1) = \frac{1}{\sqrt{2\pi}\sigma_1} e^{-\frac{(I - u_1)^2}{2\sigma_1^2}} \tag{2}$$

209

$$P_2(I, u_2, \sigma_2) = \frac{1}{\sqrt{2\pi}\sigma_2} e^{-\frac{(I - u_2)^2}{2\sigma_2^2}} \tag{3}$$

210   Where u and σ are the mean and standard deviation of the Gaussian distribution of the stain
211   intensity, respectively. In the level set approach, the level set function φ is embedded,
212   assuming $\Omega_1 = \{\varphi > 0\}$ and $\Omega_2 = \{\varphi < 0\}$, and the corresponding contour C can be represented
213   by the zero level set $\{\varphi = 0\}$. We can use the above stain intensity distribution function to
214   construct the following new SPF function:

215

$$spf(I(x)) = \frac{ln\ p_1 - ln\ p_2}{max(|ln\ p_1 - ln\ p_2|)} \tag{4}$$

216   The level set equation is:

217

$$\frac{\partial \phi}{\partial t} = spf(I(x)) \cdot \alpha |\nabla \phi| \tag{5}$$

218

219   Algorithm implementation:

220   Step 1 Initialize the level set function φ, and set the parameter α.

221   Step 2 Calculate $u_1, \sigma_1, u_2, \sigma_2$.

222   Step 3 Estimate the evolution curve through Eq. (5).

223   Step 4 $\varphi = \varphi * G_\sigma$, apply Gaussian filtering to smoothing the curve.

224   Step 5 Examine whether or not the level set function curve converges, otherwise returns to
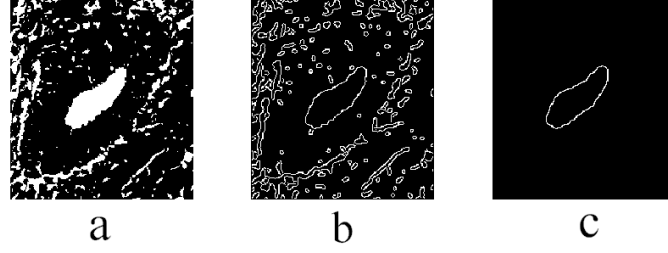225   step 2.

a   b   c

Figure 5: Extraction of lumens from the background channel. (a) The background stain intensity map; (b) The segmentation image using SPF, which contains small background areas; (c) The lumen outline after removing the small target.

The lumen segmentation process is shown in Figure 5. The lumen contour C is obtained from the background channel by the above algorithm.

We use the spatially constrained CNN (SC-CNN) for nuclear detection and the softmax CNN for nuclear sorting [35]. We use the H stain intensity map obtained from the stain separation as the input of SC-CNN to locate the nucleus. Since the detected nucleus include epithelial and stromal nucleus, nuclear sorting is used. In classification, the morphology (shape, size, color, and texture) of the nucleus is employed. Therefore, the original RGB histopathology image is selected as the input of the softmax CNN, and the pixel set V represents the epithelial cell nucleus. We select the epithelial nucleus closest to the stromal nucleus as the rough gland boundary pixels so as to obtain the rough gland boundary L.

Lumen and rough gland boundary feature representation based on the ALI (axis of least inertia).

The axis of least inertia is a line that minimizes the value after the integration of the square of the distance to all the points on the image boundary. Its physical meaning is that the rotation inertia of the graph around this axis is the smallest. It is the only reference line for representing the shape of the target. It can be known, from the physical definition of the axis of least inertia, that it must pass through the centroid O of the graph. The mathematical expression was: let the line $x + By + C = 0$, then the axis of least inertia is:

$$min \sum_{x_i, y_i \in \varphi} \frac{(x_i + By_i + C)^2}{1 + B^2} \tag{6}$$

Where φ is the set of edge points. Then we use the condition that the axis of least inertia passes the centroid $O(x_0, y_0)$: $x_0 + By_0 + C = 0$, then B and C can be obtained. In order to describe the outline of the shape, the structure-based shape descriptor commonly used in the boundary description method is mainly a chain: this is a widely used descriptor, and its role is to use the outline of the shape with directions. The chain representation of the graph: the chain represents the target by a sequence of straight lines in a given direction. If the chain is used for matching, it depends on the choice of the first boundary pixel in this sequence. From the start point of a selection, a chain sequence is generated by using the x-direction ($x = 12$, based on our experience) chain.
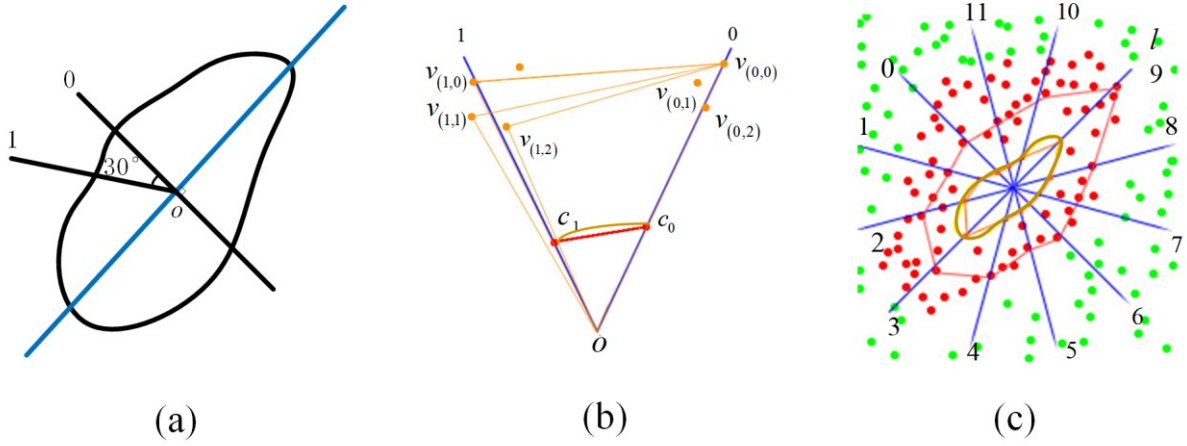
(a)　　　　　　　　(b)　　　　　　　　(c)

258

Figure 6: Feature representation approach based on the axis of least inertia .(a) The axis of least inertia is used as the reference axis. (b) Characteristic triangle. (c) The brownish yellow is the lumen contour, the orange color is the lumen contour feature triangle, and the red is one of the candidate contours obtained based on the cconstraint.

As shown in Figure 6a, the axis of least inertia is used as the reference axis, and the coordinate system is established by its perpendicular line. The lumen centroid is the origin O of the coordinate system, and then according to the direction chain, the four regions of the coordinate system are equally divided into three regions with three directions so as to generate a chain sequence with 12 directions. The direction is perpendicular to the axis of least inertia and the direction of the closest point to the lumen is 0-direction, and the counter-clockwise rotation is 30°, respectively, in the 0- to 11-direction. Then the 12 straight lines with the O point as the vertex will be compared with the lumen contour C to C_0, C_1, ..., C_{11}. 12 points constitute the chain code representing the lumen contour, and similarly the intersection points of these straight lines and the epithelial cell core set V represent candidate contour chain codes. In Figure 6b, C_0 and C_1 are the intersection of the 0- and the 1-direction and contour C, respectively, and the triangle formed by the three points C_0, C_1, O is the characteristic triangle of the lumen (the point of the lumen outline in each direction is unique). $V_{0,j}$ and $V_{1,j}$ are the intersections of the 0-, 1-direction and the epithelial nucleus set V, respectively, and the triangles formed by these points represent the gland's candidate region. There are multiple epithelial nucleus in each direction. The similarity measure is performed using a trigonometric membership function. For each feature triangle, let θ_1, θ_2, and θ_3 be the inner angles of the triangles respectively, for which they have the following relationship:

$$\mu(\theta_1,\ \theta_2,\ \theta_3)=1-\frac{1}{180}(\theta_1-\theta_3) \tag{7}$$

Then the triangular membership function:
$$\begin{cases} \theta_1 = cos^{-1}\left(\frac{d_2^2+d_3^2-d_1^2}{2d_2 d_3}\right) \\ \theta_3 = cos^{-1}\left(\frac{d_1^2+d_2^2-d_3^2}{2d_1 d_2}\right) \\ \qquad \theta_2 = 30° \end{cases} \tag{8}$$

283 Where d is the Euclidean distance between the vertices of the feature triangle. Looking at the
284 membership value of the $n\text{-}th$ feature triangle of the lumen and the membership value of the
285 $n\text{-}th$ feature triangle of the gland candidate region, the similarity between them is:

$$Sim(c,v) = \frac{\mu_n}{\mu'_n} \qquad (9)$$

287 The similarity of all the eigen values is:

$$TotalSim(c,v) = \frac{1}{n}\sum_{i=1}^{n} Sim(\mu_i, \mu'_i) \qquad (10)$$

289 If $Total\ Sim(c,v) \sim 1$, it indicates that the two contours are similar, and n represents the
290 number of the characteristic triangles.

291 The proposed approach is to find an accurate gland outline based on the two constraints:

292 The target contour S based on the epithelial nucleus set V is similar to the lumen contour C
293 and rough gland boundary L, thus constructing a feature similarity constraint:

$$\alpha \leq TotalSim(l,v) \leq 1 \qquad (11)$$

$$\beta \leq TotalSim(c,v) \leq 1 \qquad (12)$$

296 The target contour S is close to the rough gland boundary L, thus we have a distance
297 constraint:

$$s_j = \arg\min_{s_j \in v} \sum_{i=0}^{11} \left\| l_i - v_{i,j} \right\|_2 \qquad (13)$$

299 Where $i = 0,1,...,11$ represents the sequence of the directions, $j = 0,1,...,J$ represents the
300 number of the epithelial nucleus in the i-direction. l_i represents the intersection of the i-
301 direction and the rough gland boundary L, $V_{i,j}$ represent epithelial nucleus in the i-direction.
302 Taking the 0-direction as the start direction, the similarity of the feature triangles in each
303 direction is retrieved counter-clockwise. Taking Figure 6b as an example, first, the features
304 $\Delta v_{0,0}v_{1,0}o, \Delta v_{0,0}v_{1,1}o, \Delta v_{0,0}v_{1,2}o$ and the lumen feature $\Delta c_0 c_1 o$ are compared with the outer
305 contour L. The candidate contour point in direction 1 is determined by the constraint condition
306 Eqs. (13) and (14). Similarly, candidate contour points in direction 1 are used as reference
307 starting points to determine candidate contour points in direction 2. After sequentially
308 determining candidate contour points in 12 directions, this forms a candidate contour chain.
309 Assuming that there are J candidate points in the starting reference direction 0, J candidate
310 contours are formed according to the above method. In Figure 6c, the brownish yellow is the
311 lumen contour, the orange color is the lumen contour feature triangle, and the red is one of the

312 candidate contours obtained. The optimal gland contour is determined from the candidate
313 contour according to the constraint Eq. (15), and finally the gland contour is smoothed by cubic
314 spline interpolation.

Experiment Results and Discussion

Data

317 The image dataset is the Gland segmentation challenge (GLaS) dataset organized for MICCAI
318 2015 in addition to our own dataset. Our own dataset includes 100 calibrated pathological
319 images of benign and malignant colon adenocarcinoma. They were taken from 34 H & E
320 stained pathological sections of colon adenocarcinoma with cancer stage T3 or T4. Slices
321 belong to different patients, and they are processed in different laboratory environments. The
322 dataset has a very diverse diversity in a staining distribution and an organizational structure.
323 The pathological slices are scanned through the whole slice to obtain a digital picture with a
324 pixel precision of 0.465 microns. The full-frame image is readjusted to a pixel precision of
325 0.620 microns (equivalent to a 20x magnification). Then we crop them randomly to a size of

326 128× 128 and augment them to 22000 pieces for training and verification of the models. The
327 nucleus is manually annotated by an experienced pathologist. This study needs to identify
328 epithelial nucleus, so the nuclear annotation is divided into epithelial nucleus and others.

Stain separation

330 The dataset consists of 22,000 histopathology patches with the size of 128x128 each. This work
331 employs the ADAM optimizer, and the initial learning rate of 1-e3 is gradually reduced at the
332 end of each epoch. To emphasize this further, Figure 7 shows the H & E image stain separation
333 result. The results indicate that the background and H- and E-stain of histopathology images
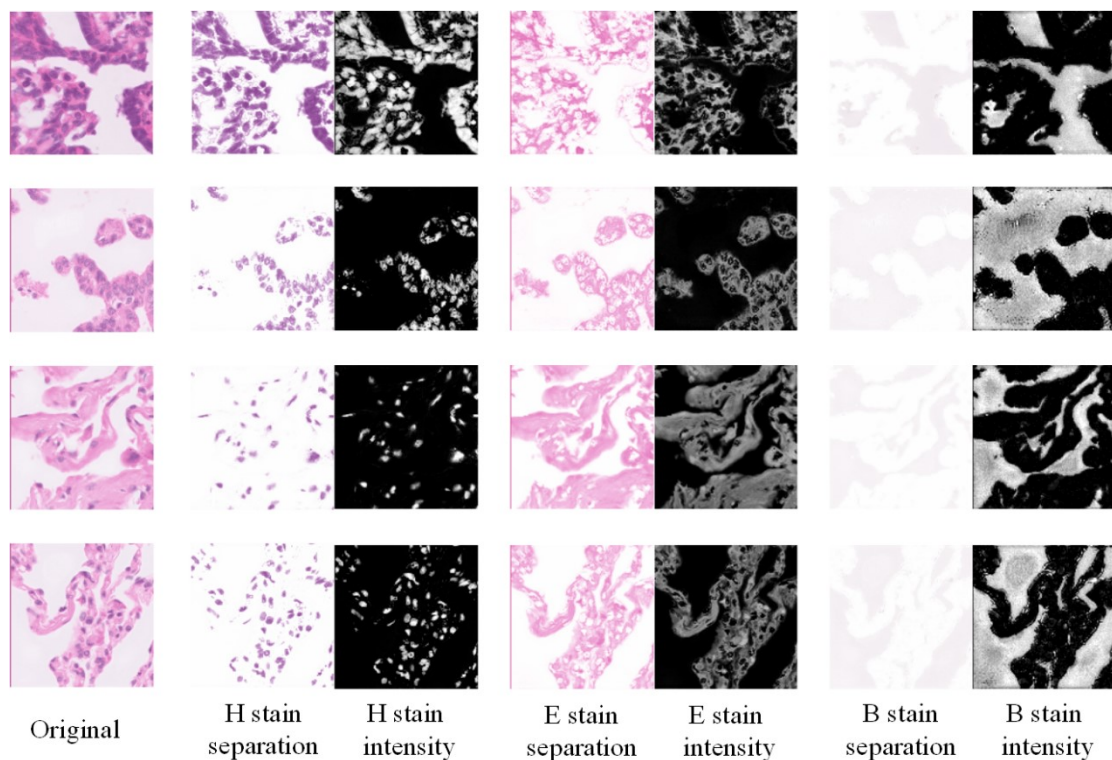334 can be successfully separated while the structure of the tissue is retained.

Original   H stain separation   H stain intensity   E stain separation   E stain intensity   B stain separation   B stain intensity

335

11

The pathological image containing the complete glandular structure is cropped without any interval to a size of 128*128, and the insufficient area was filled with zero operation. Figure 8 shows the separation results of H and E staining of the pathological images from two different datasets. The results show that for pathological images with different sources and large differences in staining, the deep learning staining separation method can successfully separate H and E stains, and the separation staining result is consistent, while maintaining the tissue structure.
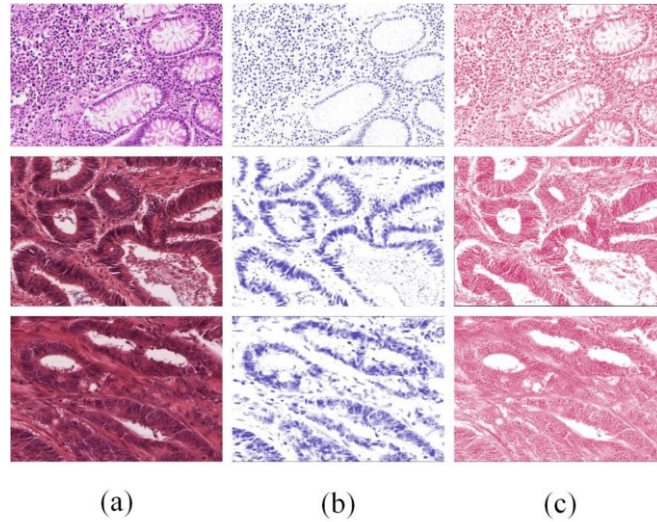

Figure 8: H&E staining and separation results of different datasets: (a) original pathological image, (b) H staining image, (c) E staining image.

After stain separation, H and E stains can be distinguished. We do not have ground truth to qualitatively evaluate the separation effect, but we can visualise the blue-violet characteristics. The H staining maps are obtained by the two traditional staining separation methods mentioned in [44] and [45], and the deep learning-based staining separation method is further investigated, and on the basis of staining separation, the cell nucleus is used to evaluate the effect of stain separation. Figure 9 shows the process of segmenting nucleus on the H-stained images. First, the H-stained image is converted into a grayscale image, then converted into a binary image as a nuclear segmentation mask, and finally the segmentation mask is overlaid on the original pathological image for us to analyze the effect of the nuclear segmentation.
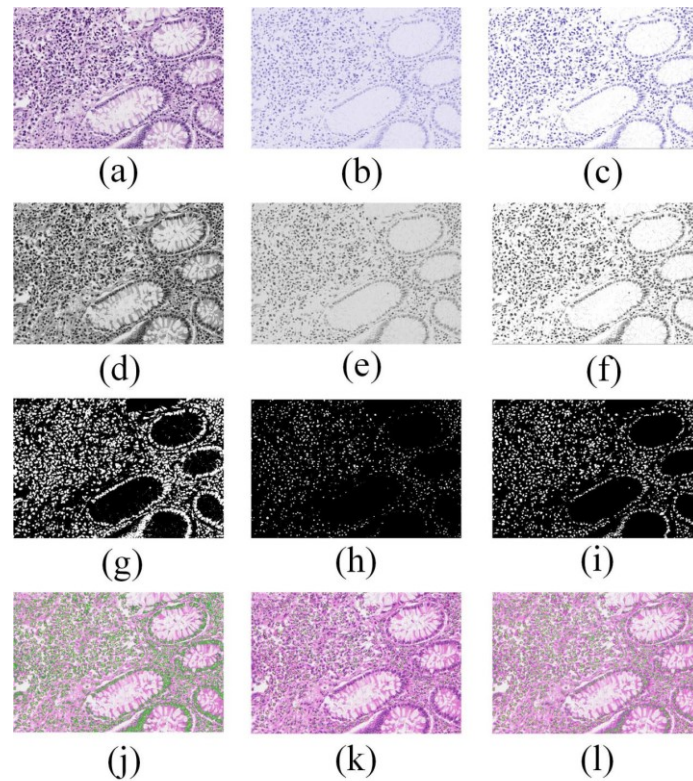
Figure 9: Nucleus segmentation of H-stain images based on three stain separation methods: (a)-(c) H-stain images based on different methods, (d)-(f) Grayscale image, (g)-(i) Binary image, (j)-(l) Segmentation mask is overlaid on the original pathological image.

A singular value decomposition method based on optical density and an independent component analysis method in the wavelet domain, two traditional methods[44-45] and the deep learning method proposed here are used to separate the same pathological tissue image, and the H stain image is used for nucleus segmentation processing, (a)-(c) in Figure 9 are the H-stained images obtained by the three stain separation methods, (d)-(f) are their corresponding grayscale images, (g)-(i) are their corresponding binary images, (j)-(l) is the outcome after we overlay the binary segmentation mask on the original image. Comparing the results (j)-(l), it can be found that (a)-(b), which have poor stain separation effects, lead to over-segmentation or under-segmentation of the nucleus.

Figure 10 shows the comparison results of different methods. The Mikto method is used for cell division, so it can only be used to isolate H staining. Color deconvolution (CD) is a classic method of stain separation, but manual intervention is required to calculate the optimal stain matrix. Using the CD method can preserve the structure, but cannot well separate the background color. SDSA is the latest method to separate stainings using statistical analysis of multi-resolution staining data. It can be seen that SDSA successfully segments H stainings, but when there are more than two stains in the image, the separation outcome is poor.
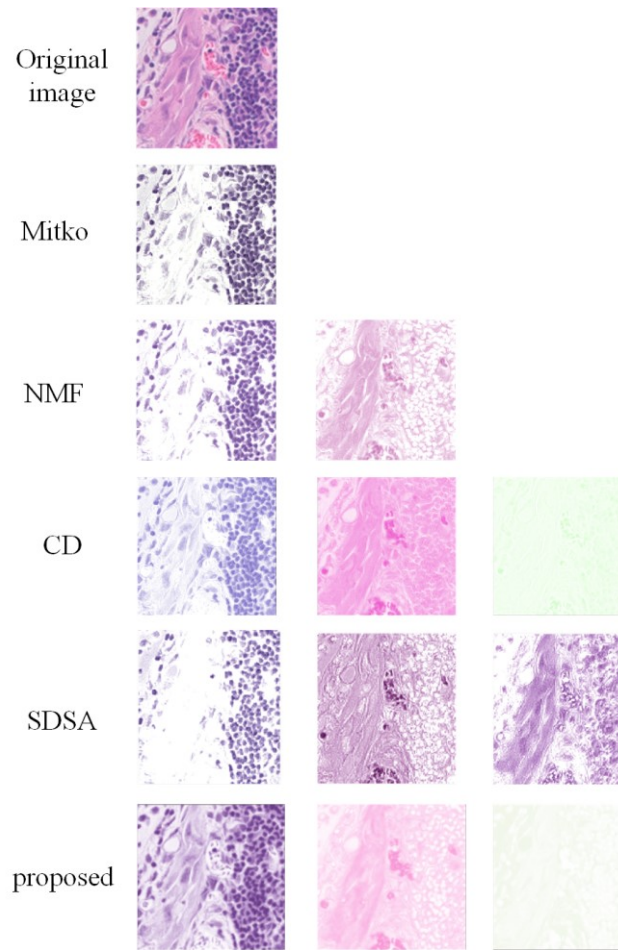
Figure 10: Comparison results against traditional methods.

Lumen segmentation

The segmentation of glands depends on the interaction between the rough gland boundary and the lumen, so it is necessary to accurately segment the lumen. In the experiment, the segmentation results of the SPF approach and the improved SPF approach on the lumens are compared. In the level set approach, for binary selection and Gaussian filter regularization, the SPF can result in satisfactory segmentation.

a   b   c   d
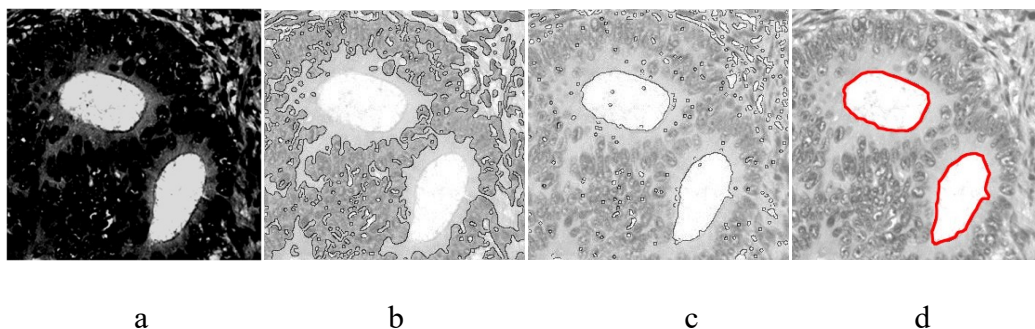
Figure 11: Segmentation of lumens based on the improved SPF approach. (a) is the background stain intensity map, (b) is the traditional SPF approach segmentation result, and it can be seen that the lumen cannot be accurately segmented, and (c) is the improved SPF approach segmentation result. (d) shows the small target has been removed.

392 Since the improved SPF approach is based on statistical information, the background channel
393 obtained from the stain separation process, in which the lumen and the background probability
394 tend to be consistent, causes some small background blocks in the image to be segmented. The
395 small target is removed from the segmented image, and the final segmentation result is shown
396 in Figure 11d.

397 Multiple segmentation techniques (e.g. DRLSE, LBF, LGDF and LIF) are used to segment the
398 glandular cavity. As shown in Figure 12, the DRLSE model produces incomplete subdivisions;
399 the LGDF model can segment the cavity from other areas. The LIF and LBF models are not
400 suitable for the segmentation of the gland cavity. These models encounter challenges such as
401 longer response time and more iterations. By using the new SPF level set segmentation method,
402 these shortcomings are overcome. The comparison results show that the proposed model is
403 easy to implement, and its calculation time is only 21 s compared with other active contour
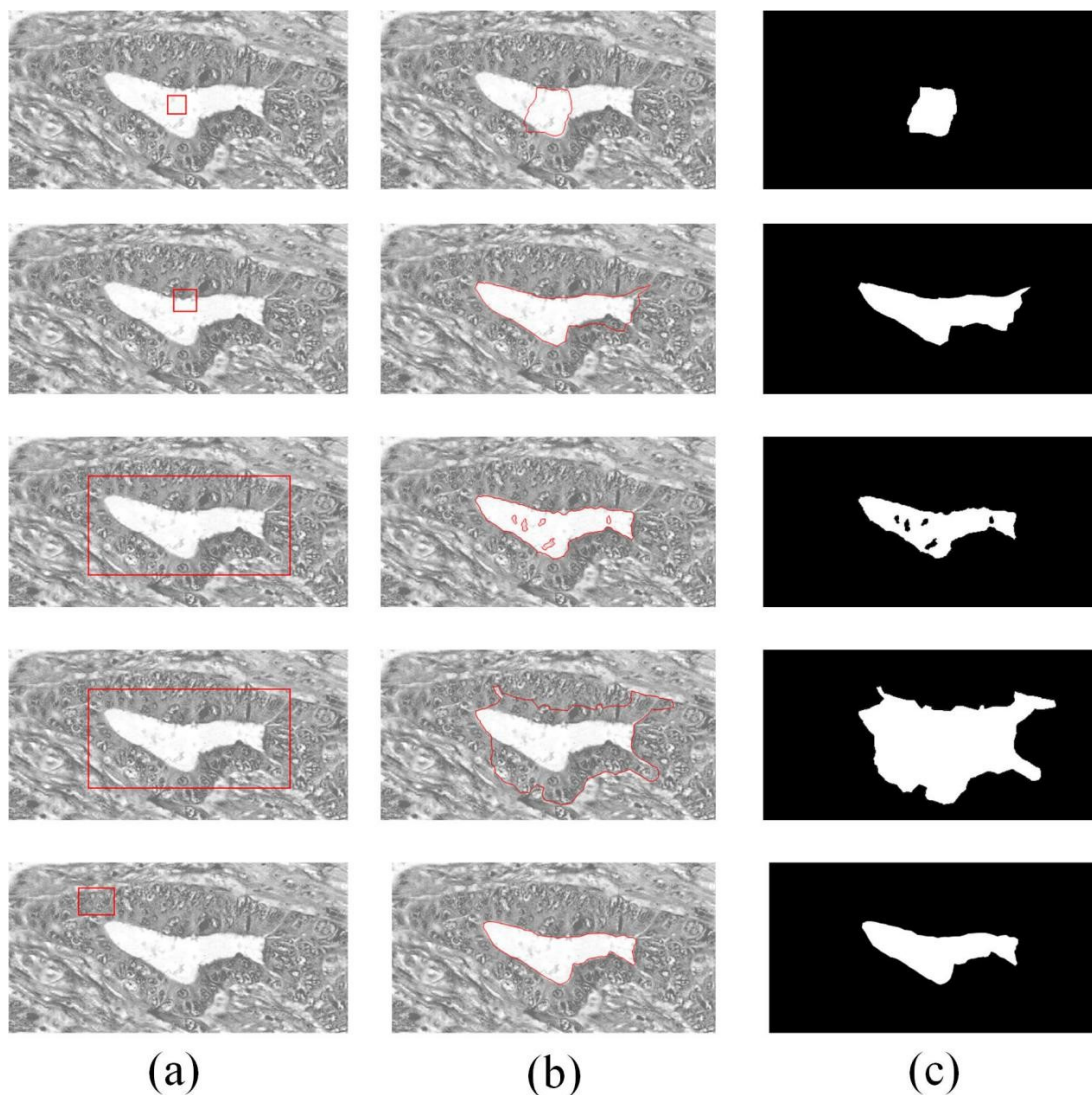404 models.

405

406 Figure 12: Segmentation of lumens using various contour models. The first row shows the results of the
407 DRLSE model, the LBF model results are shown in the second row, the third row shows the results of the
408 LGDF model, the fourth row shows the results of the LIF model, and the results of the proposed method are

15

409 shown in the fifth row. Column (a) shows the position of the initial contour. Column (b) shows the output
410 obtained after several iterations. Column (c) shows the results of gland cavity segmentation.

Gland segmentation

412 This work is evaluated on the public GlaS dataset and compared with other methods in the
413 GlaS competition. We use 100 images for system training and 65 for system testing, where 45
414 test images belong to test set A and the remaining 20 belong to test set B. For quantitative
415 analysis, we use F1 score, object Dice and object Hausdorff. Regarding Hausdorff distance,
416 lower values are better; and for other measures, higher values are better. Table 1 shows the
417 quantitative results, whereas the proposed method produces competitive results, compared with
418 those algorithms presented in the competition. The proposed-N approach is only based on
419 rough gland boundary obtained from the epithelial nucleus, and the proposed-N+L approach is
420 based on rough gland boundary N and the lumen contour *L*. The algorithm first uses deep
421 learning methods to perform staining separation. For different target segmentations, such as
422 lumens, epithelial cells, and nucleus, one can accurately segment targets on the basis of staining
423 separation. In test set A, the proposed algorithm performed poorly on F1 and the object Dice,
424 but performs better on test set B. In terms of measuring the shape similarity via object
425 Hausdorff, a lower score indicates that in malignant cases, the method takes into account the
426 effect of the morphological features of lumens, so the results have a higher shape similarity to
427 the ground truth.

428 Table 1.Comparing results of different competition algorithms on the public GlaS dataset

Method	F1 score		Object Dice		Object Hausdorff	
	Test A	Test B	Test A	Test B	Test A	Test B
Proposed-N+L	0.901	**0.851**	0.893	**0.842**	44.125	**94.528**
Proposed-N	0.886	0.816	0.886	0.823	45.236	103.686
CUMedVision1	0.868	0.769	0.867	0.800	74.596	153.646
CUMedVision2	**0.912**	0.716	**0.897**	0.781	45.418	160.347
ExB1	0.891	0.703	0.882	0.786	57.413	145.575
ExB2	0.892	0.686	0.884	0.754	54.785	187.442
ExB3	0.896	0.719	0.886	0.765	57.350	159.873
Freiburg1	0.834	0.605	0.875	0.783	57.194	146.607
Freiburg2	0.870	0.695	0.876	0.786	57.093	148.463
CVML	0.652	0.541	0.644	0.654	155.433	176.244
LIB	0.777	0.306	0.781	0.617	112.706	190.447
Vision4GlaS	0.635	0.527	0.737	0.610	107.491	210.105

429 We compare the proposed approach with the state-of-the-art algorithms
430 [17],[22],[27],[46],[47] on the our independent dataset. The relevant measurement indicators
431 are shown in Table 2. It can be seen from Table 2 that the proposed approach produces the best
432 segmentation results. Figure 13 showed the ROC curves of the different algorithms.

433 Table 2.Comparing results with the state-of-the-art algorithms.

	Accuracy (%) $\dfrac{TP+TN}{TP+TN+FP+FN}$			Dice $\dfrac{2TP}{2TP+FN+FP}$		
	Median	Mean	Std	Median	Mean	Std
Bassem et al.[17]	78.56	77.32	9.12	0.763	0.750	0.120
Sirinukunwattana et al.[22]	80.51	79.14	8.36	0.780	0.770	0.098
Linbo et al.[27]	81.11	80.48	6.52	0.801	0.795	0.089

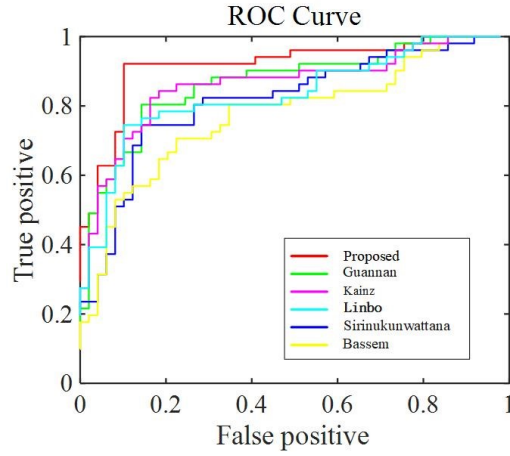|						
Kainz et al.[46]	82.53	81.08	6.13	0.825	0.815	0.076
Guannan et al.[47]	85.32	83.60	5.32	0.841	0.832	0.062
Proposed	88.34	86.91	3.72	0.874	0.869	0.047

Figure 13: The ROC curves of different algorithms.

As can be seen from Table 2, the proposed segmentation approach based on lumen and rough gland boundary improves the average pixel precision by at least 3%, and the Dice similarity coefficient has the improvement of 0.033. At the same time, the standard deviation of the pixel precision and Dice are at a low level, indicating that the segmentation approach is relatively stable and can effectively handle the problem of abnormal gland segmentation. Figure 14 shows the segmentation effect for multiple instances in our independent dataset, where green is the manually annotated contour, yellow is the segmentation contour by different methods.
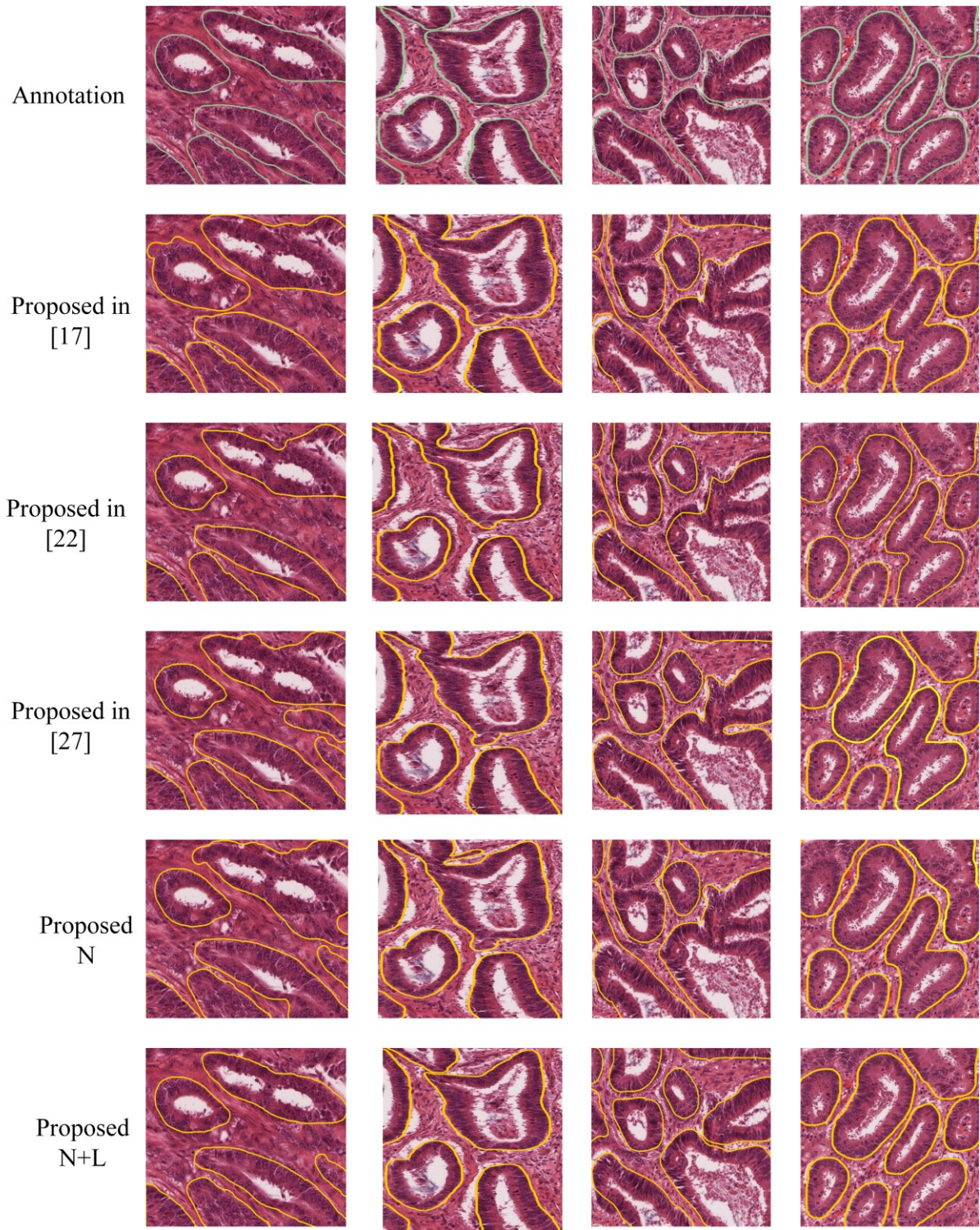
443

Figure 14: The segmentation outcomes for multiple instances on the independent dataset, where green is the manually annotated contour, yellow is the segmentation contour by different methods.

It can be seen from Fig. 14 that the gland segmentation method based only on epithelial cell nucleus, such as the one proposed in [17] and our proposed-N, relies too much on the accuracy of nuclear recognition. Inaccurate nuclear recognition directly leads to inaccurate gland segmentation. However, the method of polygonal approximation, such as the one proposed in [12], cannot detect the external contour of the gland. The double parallel structure method [27] combining the inside of the gland and the contour can segment the gland contour more

452 accurately, but sometimes it cannot segment adhering glands. In summary, for the malignant
453 and complex tumor images, our proposed method produces better segmentation results.

454 ## Conclusions

455 Histological assessment of glands is one of the challenges in colon cancer grading. Analysis of
456 histological slides stained with hematoxylin and eosin is considered to be the "gold standard"
457 in histological diagnosis. However, relying on artificial visual analysis is time consuming and
458 laborious, as pathologists need to thoroughly examine each case to ensure accurate diagnosis.
459 In order to improve the diagnostic ability of automated approaches, we here proposed an
460 approach for accurately segmenting glands in colon histopathology images based on the
461 characteristics of lumens and gland boundaries. First, this work constructed a U-net for
462 separation of H&E images to obtain H-, E-, and background stain intensity maps.
463 Subsequently, the epithelial nucleus is identified on the histopathology images, and the
464 segmentation of lumen is performed on the background intensity map. Then, the axis of the
465 least inertia and chain is used to represent the lumen and gland boundary features. Based on
466 the detection of lumens and epithelial nucleus, more accurately gland segmentation has been
467 performed based on the rough gland boundary.

468 The main contribution of the approach includes three points. Firstly, a new unsupervised stain
469 separation approach was proposed, which made the information contained in the H&E image
470 easy to identify, and deal with the uneven stain intensity and the inconspicuous stain difference.
471 The superiority of the proposed stain separation approach was proved. Second, this work
472 developed and combined a new set of features for segmentation of glands. It considered the
473 morphological characteristics of the internal lumen of the gland structure. During the process
474 of carcinogenesis, the lumen of the gland usually undergoes obvious distortion, which makes
475 the surrounding epithelial cells irregularly arranged, but most were still distributed around the
476 lumen. Therefore, the approach of combining the axis of least inertia was proposed to represent
477 the characteristics of lumens and gland boundaries. Since lumens are more independent and
478 easier to segment than the epithelial cells, the segmentation approach based on lumens can be
479 used to achieve the segmentation of glands attached to each other. The results showed that the
480 proposed approach had improved the segmentation accuracy. Finally, this work showed a
481 feature representation of lumens and gland boundaries, and we will continue to study the
482 application of this approach for benign and malignant feature extraction of tumors.

483 ## Data Availability

484 The data used to support the findings of this study were supplied by the Nantong University under
485 license and so cannot be made freely available. Requests for access to these data should be made to Kun
486 Zhang at zhangkun_nt@163.com.

487 ## Conflicts of Interest

488 The authors declares that there is no conflict of interest regarding the publication of this paper.

489 ## Funding Statement

References

[1] R Peyret , A Bouridane , F Khelifi , et al. "Automatic classification of colorectal and prostatic histologic tumor images using multiscale multispectral local binary pattern texture features and stacked generalization,"Neurocomputing 2017 .

[2] R Farjam , H Soltanian-Zadeh , K Jafari-Khouzani ,et al. "An image analysis approach for automatic malignancy determination of prostate pathological images,"Cytometr Part B,2007 .

[3] T Gultekin , C F Koyuncu , C Sokmensuer , C Gunduz-Demir . "Two-tier tissue decomposition for histopathological image representation and classification,"IEEE Trans Med Imaging 2015.

[4] R Awan, K Sirinukunwattana , D Epstein, et al. "Glandular morphometrics for objective grading of colorectal adenocarcinoma histology images," Scient Rep 2017 .

[5] R Awan , S Al-Maadeed , R Al-Saady . "Using spectral imaging for the analysis of abnormalities for colorectal cancer: when is it helpful?" PloS One 2018 .

[6]A Chaddad ,C Desrosiers , A Bouridane , et al . "Multi texture analysis of colorectal cancer continuum using multispectral imagery," PloS One 2016.

[7] K Sirinukunwattana ,JP Pluim, H Chen, et al. "Gland segmentation in colon histology images: the glas challenge contest.,"Med Image Anal 2017 .

[8] E Ahn,A Kumar,M Fulham,et al. Convolutional sparse kernel network for unsupervised medical image analysis. Medical Image Analysis,2019.

[9] Z Ding,G Fleishman,X Yang,et al. Fast predictive simple geodesic regression. Medical Image Analysis,2019.

[10]H Sokooti,G Saygili,B Glocker,et al. Quantitative error prediction of medical image registration using regression forests. Medical Image Analysis,2019.

[11]L Chen,P Bentley,K Mori,et al. Self-supervised learning for medical image analysis using image context restoration. Medical Image Analysis,2019.

[12]X Yi,E Walia,P Babyn. Generative adversarial network in medical imaging: A review. Medical Image Analysis,2019.

[13] P. Kainz et al., "Semantic segmentation of colon glands with deep convolutional neural networks and total variation segmentation," PeerJ., vol.5, 2017, Art. no. e3874.

[14] O. Ronneberger et al., "U-net: Convolutional networks for biomedical image segmentation," in Proc. Int. Conf. Med. Image Comput. Comput.-Assisted Intervention. New York, NY, USA: Springer, 2015.

[15] L.-C. Chen et al., "Deeplab: Semantic image segmentation with deep convolutional nets, atrous convolution, and fully connected CRFs," IEEE Trans. Pattern Anal., vol. 40, no. 4, pp. 834–848, Apr. 2018.

[16]K Zoltan,T Zoltan,S Sandor,et al. Colon cancer diagnosis on digital tissue images,in Computational Cybernetics,Proceedings 2013.

[17]B Ben C Philippe B Daniel,et al. "A structure-based approach for colon gland segmentation in digital pathology,"Biomedical Optics and Imaging - Proceedings of SPIE,v 9791,2016.

[18]A Banwari,N Sengar,M.K Dutta,et al."Automated Segmentation of Colon Gland Using histopathology Images,"2016 9th International Conference on Contemporary Computing, IC3 2016,March 16, 2017.

[19]A Cohen,E Rivlin,I Shimshoni,et al. "Memory based active contour algorithm using pixel-level classified images for colon crypt segmentation,"Computerized Medical Imaging and Graphics,v 43,pp150-164,July 1, 2015.

[20]K. Sirinukunwattana, D.R. Snead, N.M. Rajpoot, "A novel texture descriptor for detection of gland structures in colon histopathology images,"Biomedical Optics and Imaging- Proceedings of SPIE, v 9420,2015

[21] J.G. Jacobs, E. Panagiotaki, D.C. Alexander, "Gleason grading of prostate tumours with max-margin conditional random fields,"International Workshop on Machine Learning in Medical Imaging, Springer, 2014.

[22] K. Sirinukunwattana, D.R. Snead, N.M. Rajpoot, "A stochastic polygons model for gland structures in colon histopathology images,"IEEE Transactions on Medical Imaging,v34,n11,pp 2366-2378,November 2015.

[23] H. Fu, G. Qiu, J. Shu, et al, "A novel polar space random field model for the detection of gland structures,"IEEE Transactions on Medical Imaging,v33, n3,p764-776,March 2014

[24] H.R. Roth, L. Lu, A. Farag, et al. " Deeporgan: Multi-level deep convolutional networks for automated pancreas segmentation," International Conference on Medical Image Computing and Computer-Assisted Intervention, Springer, 2015.

[25] O. Ronneberger, P. Fischer, T. Brox, "U-net: Convolutional networks for biomedical image segmentation," International Conference on Medical Image Computing and Computer-Assisted Intervention, Springer, 2015.

[26] H. Chen, X. Qi, L. Yu, et al, "Dcan: deep contour-aware networks for accurate gland segmentation," Proceedings of the IEEE Conference on Computer Vision and Pattern Recognition, 2016.

[27] L Wang, H Zhen, X Fang, et al."A unified two-parallel-branch deep neural network for joint gland contour and segmentation learning,"Future Generation Computer Systems,v100,p316-324,November 2019

[28] Y Xu, Y Li, M Liu, et al. "Gland instance segmentation by deep multichannel side supervision," International Conference on Medical Image Computing and Computer-Assisted Intervention. Springer,2016.

[29] Y Xu, Y Li, Y Wang,et al."Gland instance segmentation using deep multichannel neural networks,"IEEE Transactions on Biomedical Engineering.v64, n12,p 2901-2912,December 2017

[30] S.E.A Raza, L Cheung, D Epstein, et al. "Gland segmentation using multi-input-multi-output convolutional neural network"Annual Conference on Medical Image Understanding and Analysis. Springer,2017.

[31] Y Zhang, L Yang, J Chen, et al. "Deep adversarial networks for biomedical image segmentation utilizing unannotated images,"International Conference on Medical Image Computing and Computer-Assisted Intervention. Springer,2017.

[32]N. Alsubaie , N. Trahearn , S.E.A. Raza , et al."Stain deconvolution using statistical analysis of multi-resolution stain colour representation,"PloS One 2017.

[33] F. Bray , J. Ferlay , I. Soerjomataram , et al."Global cancer statistics 2018: globocan estimates of incidence and mortality worldwide for 36 cancers in 185 countries," CA: Cancer J. Clin. 2018.

[34] H. Greenspan , B. Van Ginneken , R.M. Summers."Guest editorial deep learning in medical imaging: overview and future promise of an exciting new technique," IEEE Trans. Med. Imaging 2016.

[35]K Sirinukunwattana,R Ahmed, E Shan, et al. "Locality Sensitive Deep Learning for Detection and Classification of nucleus in Routine Colon Cancer histopathology Images,"IEEE Transactions on Medical Imaging,v35, n5,p 1196-1206,May 2016

[36]C Li,J Su,L Yu,et al. "A variational level set approach image segmentation model with application to intensity inhomogene magnetic resonance imaging,"Multimedia Tools and Applications,v77,n23,p 30703-30727,December 1, 2018.

[37]G-G Carlos, S-RM Luisa, C-RJ Luis, et al. "Multi-GPU Development of a Neural Networks Based Reconstructor for Adaptive Optics," Complexity, 2018.

[38]C Xin, Y Zuyuan, Y Chao, et al. "Sparse Gene Coexpression Network Analysis Reveals EIF3J-AS1 as a Prognostic Marker for Breast Cancer,"Complexity, 2018.

[39]G Tatjana, S Zoran, M Branislav, et al. "Follow-Up and Risk Assessment in Patients with Myocardial Infarction Using Artificial Neural Networks,"Complexity, 2017.

[40]R V Sol, R Ferrer-Cancho, J M Montoya, et al. "Selection, tinkering, and emergence in complex networks,"Complexity, 2002.

[41] Z. Han , B. Wei , Y. Zheng , et al."Breast cancer multi-classification from histopathological images with structured deep learning model,"Sci.Rep.2017.

[42] S. Hussain , S. Saxena , S. Shrivastava , et al."Multiplexed autoantibody signature for serological detection of canine mammary tumours," Sci. Rep.2018.

[43]T F Chan,L A Vese."Active Contours without Edges,"IEEE Transactions on Image Processing,v 10, n 2,p 266-277,Feb 2001.

[44]M Macenko ,M Niethammer ,JS Marron,et al.A method for normalizing histology slides for quantitative analysis.2009 IEEE International Symposium on Biomedical Imaging:From Nano to Macro.p1107-1110,2009.

[45]N Alsubaie ,R Shan ,N Rajpoot .Stain deconvolution of histology images via independent component analysis in the wavelet domainIEEE,International Symposium on Biomedical Imaging.IEEE,2016.

[46] K Philipp,P Michael,U Martin. "Segmentation and classification of colon glands with deep convolutional neural networks and total variation regularization,"PeerJ,2017.

[47]G Li,E Shan,A Raza,et al."Multi-resolution cell orientation congruence descriptors for epithelium segmentation in endometrial histopathology images,"Medical Image Analysis,v 37,p 91-100,April 1, 2017

[48] S. Hussain , S. Saxena , S. Shrivastava , et al."Gene expression profiling of spontaneously occurring canine mammary tumours: insight into gene networks and pathways linked to cancer pathogenesis," PloS One 2018.

[49] P. Khosravi , E. Kazemi , M. Imielinski , et al."Deep convolutional neural networks enable discrimination of heterogeneous digital pathology images,"EBioMedicine 2018.

[50] P. Sudharshan , C. Petitjean , F. Spanhol , et al."Multiple instance learning for histopathological breast cancer image classification," Expert Syst.2019.

[51]S.K. Zhou , H. Greenspan , D. Shen ."Deep Learning for Medical Image Analysis,"Academic Press, 2017 .

[52]M Arsalan , D S Kim,M B Lee,et al. "FRED-Net: Fully residual encoder-decoder network for accurate iris segmentation." Expert Systems and Application, 2019.

608　　[53]M Arsalan, R. A. Naqvi,D. S Kim, et al.“IrisDenseNet: Robust iris segmentation using densely connected
609　　　　　fully convolutional networks in the images by visible light and near-infrared light camera sensors.” Sensors,
610　　　　　2018.